4

Adaptive Beamforming by Phase Coherence Processing

J. Camacho and C. Fritsch
Consejo Superior de Investigaciones Científicas (CSIC), Madrid
Spain

1. Introduction

The quality of *phased array* and *synthetic aperture* ultrasonic images is limited by several factors determined by the sound propagation physics and diffraction laws. Image quality is mainly determined by:

1. *Resolution*, which depends on signal bandwidth (in the axial direction) and on the aperture extent (in the lateral direction).
2. *Dynamic range*, which is bounded by the ratio of the main to the sidelobes level and is related to the smallest features detection capability.
3. *Contrast*, which is the capability to differentiate among subtle changes in the acoustic impedance (i.e., different tissues in medical imaging).
4. *Signal-to-noise ratio*, where noise can be electrical (i.e., thermal, EMI, etc.) or *speckle*, also called *clutter* or *grain noise*, depending of the application field. Speckle results from interferences among unresolved *scatterers* in a *range cell*.
5. *Artifacts,* such as *reverberations*, *grating lobes* and others which blur the image and reduce the dynamic range.

Along the years, many research efforts have been devoted to find techniques that increase the image quality by addressing the above factors. Frequently, some characteristics are improved at the expenses of losses in some others. A typical example is *apodization*, used to reduce the sidelobe level, with an adverse effect in the lateral resolution [Szabo, 2004]. In medical imaging, where contrast is essential, this function is quite useful; however, in the NDT field, where resolution is more relevant, apodization provides marginal or no benefits at all.

As another example, lateral resolution is improved with larger apertures, which may be obtained with increased array inter-element pitch d. However, when $d>\lambda/2$ (*sparse apertures*) grating lobe artifacts appear. The condition $d>\lambda/2$ also arises with 2D arrays or in high frequency ultrasound imaging due to manufacturing constraints. Sparse apertures with randomly distributed elements reduce the grating lobes by spreading their energy among the sidelobes, whose level increases [Turnbull & Foster, 1991]; [Gavrilov et al., 1997].

In other cases, the concept of *effective aperture* allows to reduce the grating lobe levels by using different element distributions in emission and in reception, so that the compound radiation pattern equals that of a dense aperture [Lockwood et al., 1998]; [Nikolov & Jensen, 2000]; [Nikolov & Behar, 2005]. When a single focus is set in emission (as in phased array), some residual grating lobe artifacts remain in the image [Lockwood et al., 1996]. Furthermore, these approaches produce a lower signal-to-noise ratio.

As a final case example, speckle noise can be reduced by image compounding (*spatial diversity*), but this negatively affects resolution [Shankar & Newhouse, 1985]. *Frequency diversity* methods have been also proposed [Newhouse et al., 1982], but they critically depend on the selected parameters to work properly [Gustafson & Stepinski, 1993].
The conclusion is clear: there is no a *universal* method to improve the image quality by simultaneously addressing all the involved factors. This work is an exception to this rule, where *simultaneous improvements* in lateral resolution, side and grating lobe suppression, signal-to-noise ratio enhancement and artifacts cancellation, with the corresponding improvements on contrast and dynamic range, are obtained.
This is achieved by a new ultrasound imaging concept: *Adaptive Beamforming by Phase Coherence Processing*. The idea behind this approach is to consider the aperture data phases *explicitly* in the image formation process [Camacho et al., 2009].
Until now, this has not been applied in conventional ultrasonic imaging, whatever is the modality (phased array or synthetic aperture). Rather, the aperture data phases are only implicitly involved in the coherent sum, thus disregarding relevant information for the image formation. The aim of this work is to give the basis of the new technique and show its performances both, with simulated and experimental data.

2. The aperture data phases

The beamforming process is achieved by introducing delays that compensate the differences in the round-trip time-of-flight from the emitter to the focus and to every element. In the phased array modality, the emitter is considered at the array center, whereas in synthetic aperture imaging the actual emitter position is used to compute the delays. This way, dynamic focusing can be performed in reception only (phased array) or in emission and reception (synthetic aperture imaging).
From the simple geometry of Fig. 1, the round-trip time-of-flight from the array center O to the focus F and to element X is:

$$t_i^p = \frac{R_f + \left|\vec{r}_f\right|}{c} = \frac{1}{c}\left(R_f + \sqrt{R_f^2 + x_i^2 - 2R_f x_i \sin\theta}\right) \tag{1}$$

where c is the sound propagation velocity. The delay applied to signals received by element i for focusing at F is:

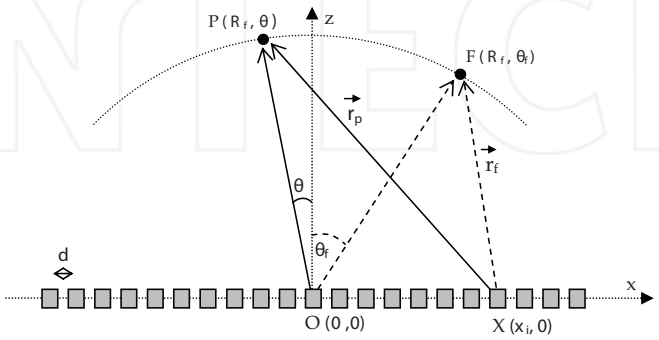

Fig. 1. Geometry for computing the focusing delays.

$$\tau_i = \frac{1}{c}\left(R_f - \sqrt{R_f^2 + x_i^2 - 2R_f x_i \sin\theta_f} \right) \quad 1 \le i \le N \tag{2}$$

Considering an emitted signal $e(t)=E\cdot\cos(\omega_s t)$, with $\omega_s=2\pi f_s$, the *aperture data* $s_i(t)$ that results after application of the focusing delay τ_i to the signal received by element i is:

$$s_i(t) = E\cos\left(\omega_s t - \omega_s \left(t_i^P + \tau_i \right) \right) \tag{3}$$

and the *unwrapped phase* of the aperture data i is:

$$\Phi_i(t) = \omega_s t + \frac{\omega_s}{c}\sqrt{R_f^2 + x_i^2 - 2R_f x_i \sin\theta_f} - \frac{\omega_s}{c}\sqrt{R_f^2 + x_i^2 - 2R_f x_i \sin\theta} \tag{4}$$

With the approximation $(1+a)^{1/2} \approx 1+a/2$, for a small and, with $R_f >> x_i$,

$$\Phi_i(t) \approx \omega_s t + \frac{\omega_s}{c} x_i \left(\sin\theta_f - \sin\theta \right) \tag{5}$$

The term $\omega_s t$ is equal for all the elements at a given time instant, so that the variability of the set $\{\Phi_i\}$ is only determined by the second term. On the other hand, for an N-element linear array with the coordinate origin at its center and inter-element spacing d,

$$x_i = [i - (N+1)/2]d \qquad 1 \le i \le N \tag{6}$$

Substituting in (5) and ignoring the time-dependent term:

$$\Phi_i \approx \frac{\omega_s d}{c}[i - (N+1)/2]\left(\sin\theta_f - \sin\theta \right) \tag{7}$$

Thus, for a point reflector at P (R_f, θ) with $\theta \neq \theta_f$, the unwrapped phases vary linearly along the aperture data. Only if P is located at the focus F ($\theta = \theta_f$), all the phases become equal.
Therefore, by analyzing the dispersion of the aperture data phases, it can be realized when the received signals come from the focus or from some other region. To this purpose, any measurement of the statistical dispersion of the aperture data phases can be used (standard deviation, variance, etc.). For example, the standard deviation σ_Φ of the set of aperture data phases $\Phi = \{\Phi_i\}$ is computed from:

$$\sigma_\Phi = \sqrt{\frac{1}{N}\sum_{i=1}^{i=N}\left(\Phi_i - \frac{1}{N}\sum_{i=1}^{i=N}\Phi_i \right)^2} \tag{8}$$

After some mathematical manipulation, substitution of (7) in (8) yields,

$$\sigma_\Phi(\theta) = std(\Phi) = \frac{\pi}{\sqrt{3}}\frac{d}{\lambda}\sqrt{N^2-1}\left| \sin\theta_f - \sin\theta \right| \tag{9}$$

For $N>>1$ and with $D=N\cdot d$,

$$\sigma_\Phi(\theta) \approx \frac{\pi}{\sqrt{3}}\frac{D}{\lambda}\left| \sin\theta_f - \sin\theta \right| \tag{10}$$

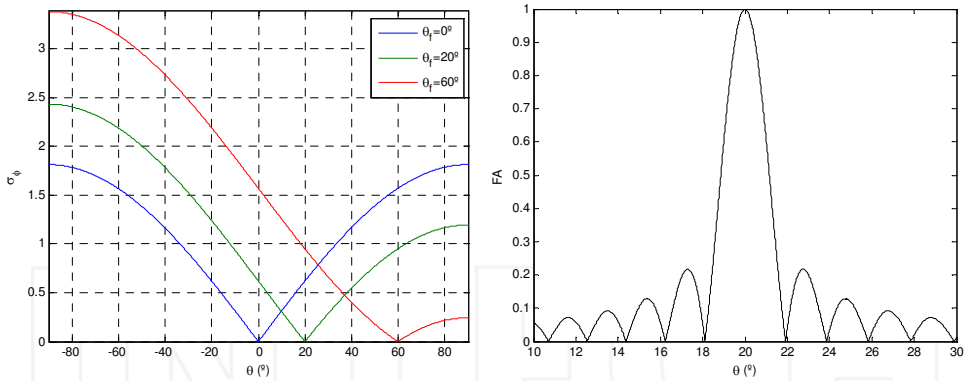

Fig. 2. Left: plot of σ_Φ in D/λ units for three steering angles. Right: $FA(\theta)$ around $\theta_f = 20^o$.

Figure 2 (left) shows this function for three steering angles θ_f in D/λ units. It is seen that σ_Φ is zero only at the focusing direction, showing increasing values as θ separates from θ_f. This can be used to detect signals strictly coming from the focus ($\sigma_\Phi = 0$) or, with a more practical point of view, from *inside* the array main lobe.
The normalized radiation pattern of an array in continuous wave is[Steinberg, 1976]:

$$FA(\theta) = \left| \frac{\sin\left[\frac{\pi D}{\lambda}\left(\sin\theta_f - \sin\theta\right)\right]}{\sin\left[\frac{\pi d}{\lambda}\left(\sin\theta_f - \sin\theta\right)\right]} \right| \tag{11}$$

which is zero at

$$\sin\theta_{Zn} = \sin\theta_f \pm \frac{\lambda}{D} n \qquad n = 1, 2, ... \tag{12}$$

and unity at $\theta=\theta_f$. Figure 2 (right) shows an example for $D=32\lambda$, $d=\lambda/2$. The main lobe is bounded by the first zeroes of the radiation pattern (n=1) at:

$$\sin\theta_{z1} = \sin\theta_f \pm \lambda / D \tag{13}$$

Substitution of this value for $\sin\theta$ in (10) yields:

$$\sigma_\Phi\left(\theta_{z1}\right) = \frac{\pi}{\sqrt{3}} \tag{14}$$

Therefore, if the standard deviation of the aperture data unwrapped phases is $0 \le \sigma_\varphi \le \pi/\sqrt{3}$, it can be assumed that the received signals were originated inside the main lobe. This leads to a straightforward method for suppression of the side lobes, as it is explained next. The value $\sigma_0=\pi/\sqrt{3}$ equals the standard deviation of a uniform linear distribution in $(-\pi, \pi]$.

3. Phase coherence factors

The absolute phase coherence factor (*FCA*) is defined to take values in the [0, 1] interval as a function of the standard deviation of the aperture data unwrapped phases:

$$FCA = \max\left(0\ ,1-\frac{\sigma_\Phi}{\sigma_0}\right) \tag{15}$$

The term $f = 1\text{-}\sigma_\Phi/\sigma_0$ takes the unity at the main lobe axis, where $\sigma_\Phi=0$, then monotonically decreases reaching zero at the main lobe limits θ_{z1}, where $\sigma_\Phi= \sigma_0$, and continues decreasing with negative values for angles θ outside the main lobe, where $\sigma_\Phi > \sigma_0$. As the function max(0, f) avoids negative values, the *FCA* is zero in the latter region (at the side lobes).
Figure 3a shows $FCA(\theta)$ over the normalized radiation pattern. It can be appreciated that the coherence factor has a narrower main lobe than the array factor and is free of side lobes. However, both reach unity at the focus steering angle θ_f.
In any conventional digital beamformer, the output is the coherent sum of the aperture data:

$$y(k) = \sum_{i=1}^{N} s_i(k) \tag{16}$$

where k is the sample index. Suppression of sidelobes can be achieved by weighting the beamformer output with the coherence factor obtained from the k-th aperture data set:

$$z(k) = y(k) \cdot FCA(k) \tag{17}$$

Besides suppressing sidelobes, this operation provides a narrower main lobe as shown in Figure 3b (compare, for example, the original and resulting main lobe width at -6 dB).

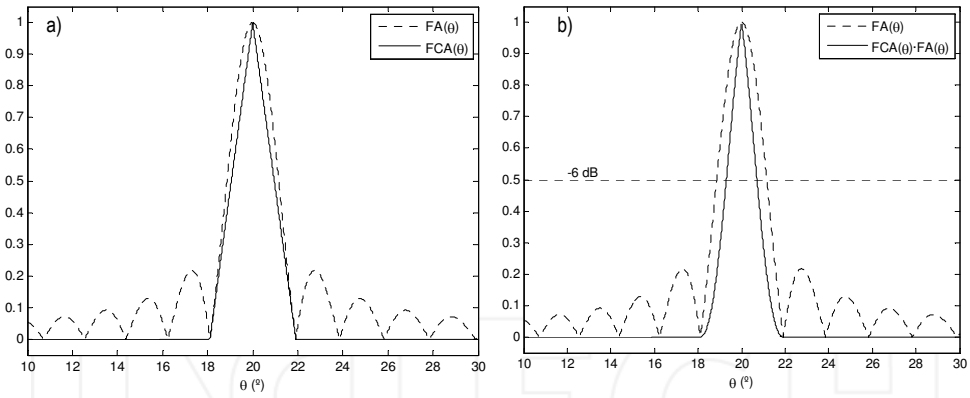

Fig. 3. a) $FCA(\theta)$ and FA(θ) for $\theta_f = 20^o$; b) Radiation pattern after the weighting operation

However, the unwrapped phase is not usually available. Instead, the *instantaneous phase* (wrapped phase) can be obtained from the signal analytical representation of the aperture data, $S_i(k) = Ae^{j\varphi_i(k)} = SI_i(k) + jSQ_i(k)$ as:

$$\varphi_i(k) = \tan^{-1}\left(\frac{SQ_i(k)}{SI_i(k)}\right) \tag{18}$$

being SQ and SI the quadrature and in-phase components, respectively. With $SI_i(k) = s_i(k)$, $SQ_i(k)$ can be obtained by means of a Hilbert transform, $SQ_i(k) = Hilbert[s_i(k)]$, [Oppenheim &

Schaffer, 1989], or by any other approximate process [Ranganathan et al., 2004]. If the former is used, the instantaneous phases can be obtained from the aperture data by:

$$\varphi_i(k) = \tan^{-1} \frac{Hilbert[s_i(k)]}{s_i(k)} \tag{19}$$

Then, the unwrapped phases Φ_i can be evaluated from φ_i. A common unwrapping algorithm scans the vector φ_i from i=2 to N, computing the increments $\Delta\varphi_i = \varphi_i - \varphi_{i-1}$; when $|\Delta\varphi_i| > \pi$, a value of sign($\Delta\varphi_i$)·2π is subtracted to the successive phases, from i to N.
However, it is also possible to avoid the unwrapping process by using the value of the instantaneous phases to evaluate a different coherence factor. In this case, since the phases are circularly distributed in the (-π, π] interval, a different function to obtain the standard deviation should be used [Fisher, 1993].
But, also, the circular distribution of the instantaneous phases can be considered that of vectors in the unit circle (module=1, angle=φ_i), represented as the complex cosφ_i + $j$sinφ_i. The standard deviation of a complex number σ_c is computed as the square root of the sum of the variances of the real and imaginary parts, that is:

$$\sigma_c = \sqrt{\mathrm{var}(\cos\varphi_i) + \mathrm{var}(\sin\varphi_i)} \tag{20}$$

In this case, $0 \le \sigma_c \le 1$, so that the complex phase coherence factor, *FCC* can be defined as:

$$FCC = 1 - \sigma_c \tag{21}$$

Furthermore, to avoid the complications involved in computing σ_c in the complex plane, it is possible to consider the phase having a linear distribution in the (-π, π] interval. In such case,

$$\sigma_\phi = \sqrt{\frac{1}{N}\sum_{i=1}^{i=N}\left(\varphi_i - \frac{1}{N}\sum_{i=1}^{i=N}\varphi_i\right)^2} \tag{22}$$

However, it must be taken into account that, when the phases become grouped around φ=±π, a large σ_φ will be produced in spite of being very similar phases, a consequence of considering the phase a linear distribution. A general solution to this problem is given later.
When phases distribute uniformly in the (-π, π] interval, the standard deviation is σ_0=π/$\sqrt{3}$. This happens when signals are just white noise and, approximately, at the sidelobes. This way, analogously to the *FCA*, the linear phase coherence factor *FCF* is defined as:

$$FCF = \max\left(0\,,\,1 - \frac{\sigma_\varphi}{\sigma_0}\right) \tag{23}$$

4. Comparison of phase coherence factors

The phase coherence factors *FCA*, *FCC* and *FCF* share, in general, the same properties of sidelobe suppression and main lobe narrowing, but with some important differences. So, at the sidelobes, $\sigma_\varphi \approx \sigma_0 = \pi/\sqrt{3}$, which provides a *FCF*(θ) *near zero*, but with some small positive spikes at angles where $\sigma_\varphi < \sigma_0$. At angles where $\sigma_\varphi > \sigma_0$, it is $f = 1-\sigma_\Phi/\sigma_0 < 0$ and the function max(0, f) nulls the *FCF*. This behavior contrasts with that of *FCA*(θ), which is zero at the sidelobes, achieving their complete suppression (Fig. 4).

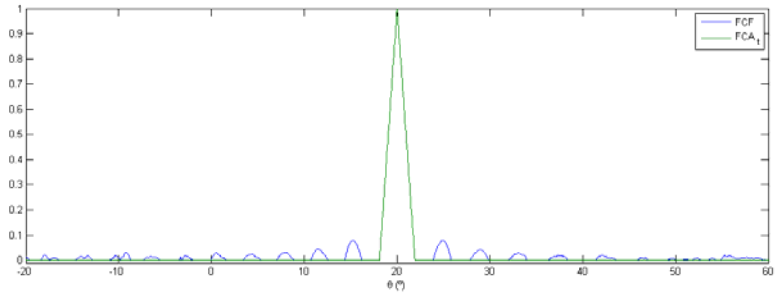

Fig. 4. Comparison among $FCF(\theta)$ and $FCA(\theta)$ for $\theta_f = 20^o$.

Another difference is a consequence of considering the instantaneous phases linearly distributed in $(-\pi, \pi]$. The effect is critical when the focus is located at an odd multiple of $\lambda/2$, where the standard deviation is zero just at θ_f since all phases are exactly π, but at angles $\theta \approx \theta_f$ (at both sides of the main lobe axis), phases group around $\varphi=\pm\pi$, producing a large σ_φ. Figure 5 compares $\sigma_\varphi(\theta)$ when the focus is located at an even or odd multiple of $\lambda/2$. This periodic effect appears in the image as a pattern, an artifact that must be avoided.

The complex coherence factor $FCC(\theta)$ does not present phase discontinuities and shows a smooth pattern. Figure 6 compares $FCC(\theta)$ with $FCF(\theta)$ for a focus at an even multiple of $\lambda/2$. The latter shows irregularities caused by the phase discontinuities that are not present in $FCC(\theta)$. Furthermore, the FCC provides higher side lobe suppression and a slightly narrower main lobe, whose width is independent of the focus axial position. The irregularities shown by $FCF(\theta)$ in the sidelobes region are of low level and, thus, have little impact on the image.

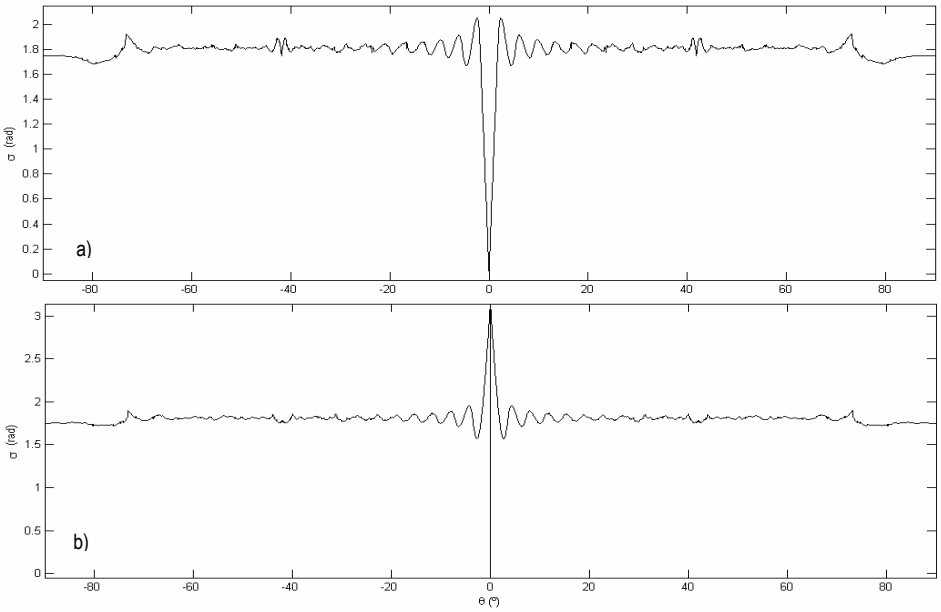

Fig. 5. Plot of $\sigma_\varphi(\theta)$: a) Focus at an even multiple of $\lambda/2$; b) Focus at an odd multiple of $\lambda/2$.

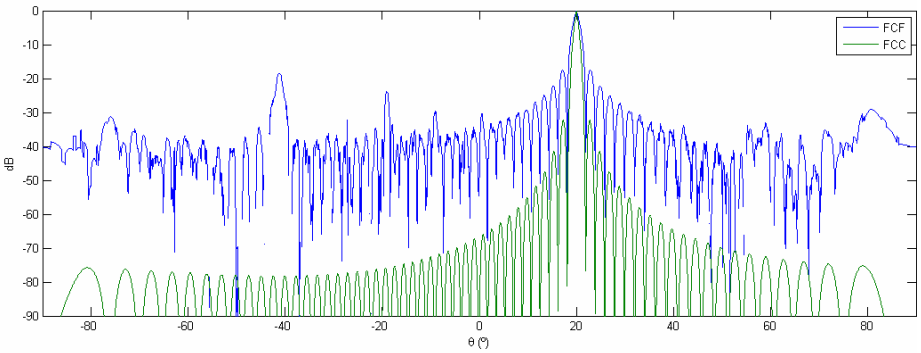

Fig. 6. Comparison between $FCC(\theta)$ and $FCF(\theta)$.

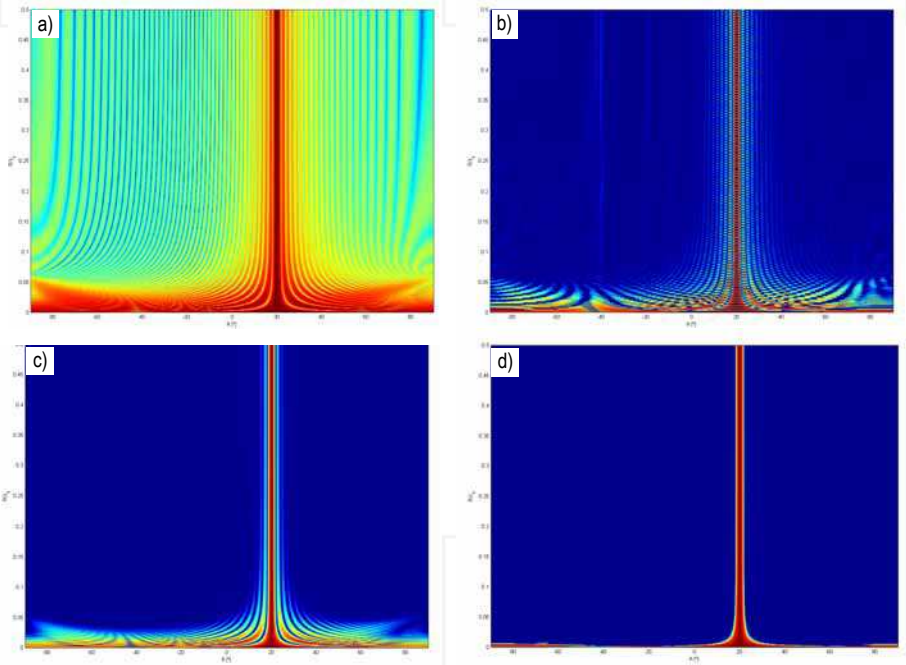

Fig. 7. Reception patterns: a) Conventional beamforming; b) Weighted by *FCF*; c) Weighted by *FCC*; d) Weighted by *FCA*. Dynamic range = 70 dB. Array: N=64, d= λ/2, θ_f = 20º.

Figure 7 shows the *reception pattern* with a 70 dB of dynamic range, considering continuous omnidirectional emission from the array center and dynamic focusing in reception, for an array with N=64 elements, d= λ/2 and processing with different coherence factors.
The side lobe indications shown by the original image in (a) become mostly suppressed with the phase coherence processing, whatever is the coherence factor used. However, weighting the beamformer output with the *FCF* (in b) produces the periodic pattern in the propagation direction discussed before. Also, some residual sidelobe indications remain.

In (c) the beamformer output is weighted with *FCC*, which shows a smooth beam without periodic artifacts and with higher sidelobe suppression. However, some sidelobe indications remain in the very near field (below 1/20 the far field limit) and near the main lobe (the first sidelobes), in agreement with the results shown in Fig. 6.
Finally, processing with the *FCA* (d) provides full sidelobe suppression, even in the very near field region, and a uniform main lobe pattern, which does not depend on depth.
These results have been obtained under the assumption of monochromatic wave and noise-free signals. The effect on wideband signals with noise is analyzed in the next Sections.

5. Phase quantization and the sign coherence factor FCS

In any digital implementation of the proposed method, the phase will be quantized. It is relevant to consider the errors involved as a function of the resolution used to represent the phases. Figure 8 shows the rms error in the computed *FCF* when the phase is quantized with a number *B* of bits, with regard to a 64-bits floating point representation.

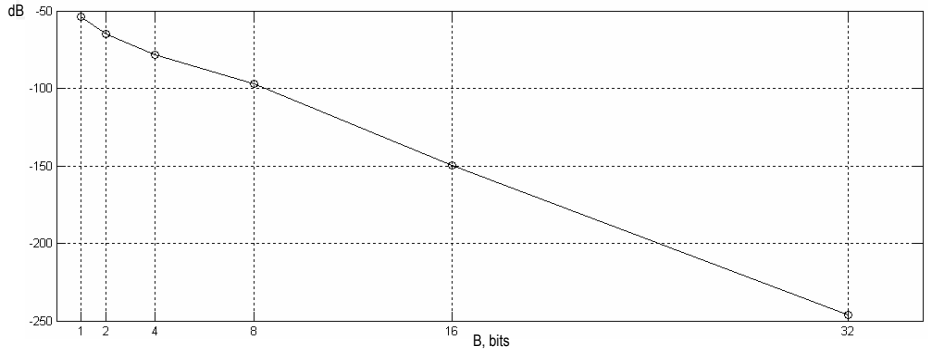

Fig. 8. *FCF* rms error as a function of the number of bits used to represent the phases.

It becomes apparent that the *FCF* is not very sensitive to the phase resolution. In fact, the rms error of computing the phases with only 4 bits instead of 64 bits is lower than 0.1%. In an extreme case, the phase can be coded with a single bit by breaking the $(-\pi, \pi]$ interval in:

$$\Psi_i(k) = \begin{cases} \pi/2 & \text{for } \varphi_i(k) \in [0, \pi] \\ -\pi/2 & \text{for } \varphi_i(k) \in (-\pi, 0) \end{cases} \tag{24}$$

For received signals of the form $s(t) = A(t)\sin(\varphi(t))$, with $A(t)>0$, these intervals correspond to the sign of $s(t)$, represented here by the discrete variable $b_i(k)$:

$$b_i(k) = \begin{cases} +1 & \text{for } s_i(k) \geq 0 \\ -1 & \text{for } s_i(k) < 0 \end{cases} \tag{25}$$

The variance of this variable is (omitting the sample index k):

$$\sigma_b^2 = \frac{N \sum_{i=1}^{N} b_i^2 - \left(\sum_{i=1}^{N} b_i \right)^2}{N^2} \tag{26}$$

and, since $\sum b_i^2 = N$,

$$\sigma_b^2 = 1 - \left(\frac{1}{N} \sum_{i=1}^{N} b_i \right)^2 \tag{27}$$

The Sign Coherence Factor, *FCS*, is defined as a function of the standard deviation of the aperture data signs:

$$FCS = 1 - \sigma_b = 1 - \sqrt{1 - \left(\frac{1}{N} \sum_{i=1}^{N} b_i \right)^2} \tag{28}$$

The sign coherence factor also takes values in the [0, 1] interval since $\sigma_b \leq 1$. One advantage of this function is its low computing cost, which allows a simple hardware implementation.
Figure 9 (left) shows $FCS(\theta)$ for an steering angle $\theta_f = 30^o$. It reaches unity around the focus in the region where all the signals have the same polarity. Outside of this angular interval, $FCS(\theta)$ approaches zero.
The result of weighting the beamformer output with the sign coherence factor is shown in Figure 9 (right), together with the original radiation pattern. Both are equal around the steering angle, falling to low values (below -40 dB) at the sidelobe region. Note that the first sidelobe has been reduced by more than 26 dB and, simultaneously, the main lobe becomes narrower. The small irregularities in the resulting pattern are due to the discrete nature of the sign, but they have little impact on the image.

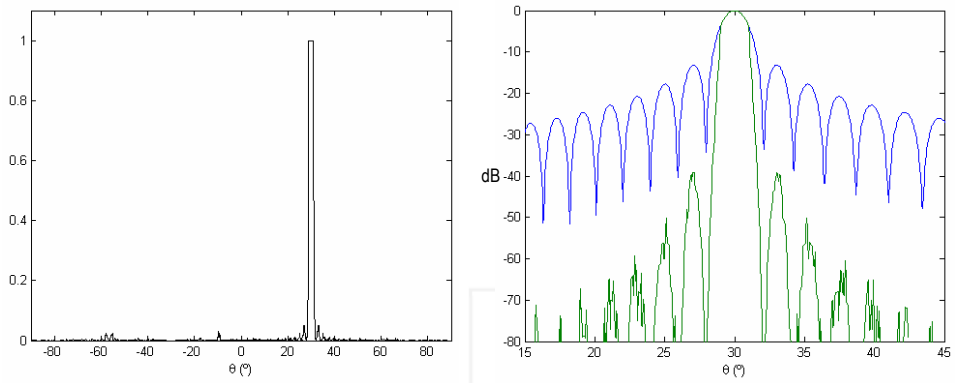

Fig. 9. Left: $FCS(\theta)$; Right: $FA(\theta)$ before (blue) and after (green) weighting by $FCS(\theta)$.

The $FCS(\theta)$ is a particular case of the $FCF(\theta)$, where the phases have been quantified with 1 bit. Therefore, it also shows the dependence with the focus position in the axial direction. In this case, the spatial period is $\lambda/2$, instead of λ.
Figure 10(a) shows the original reception pattern with a 70 dB of dynamic range, for an array with N=64, d= $\lambda/2$ and a steering angle at $\theta_f = 20^o$ (the same case shown in Fig. 7a). The sidelobe indications become nearly suppressed when the beamformer output is weighted with the *FCS*, with residual values below -70 dB, as shown in (b). However, the image shows the periodic artifact caused by the dependence of $FCS(\theta)$ with the focus position, similar to that shown by $FCF(\theta)$ (see Fig. 7b), but of higher spatial frequency.

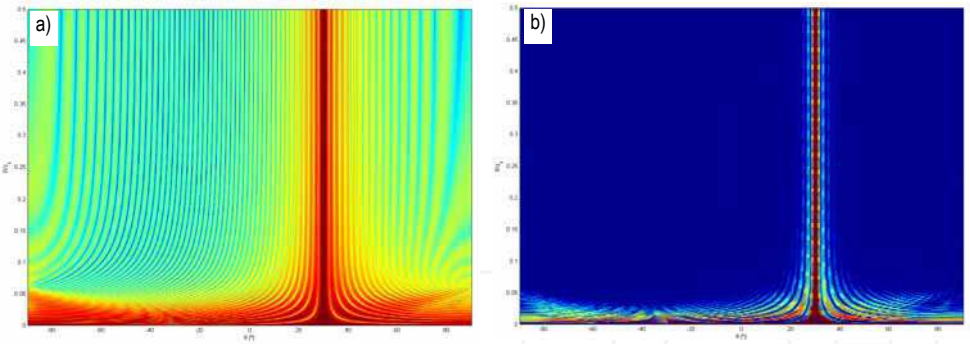

Fig. 10. Reception patterns: a) Conventional beamforming; b) Weighted by *FCS*. Image dynamic range = 70 dB. Array: N=64, d= $\lambda/2$, θ_f = 20º.

6. Wideband and noisy signals

Until now, monochromatic and noise-free signals have been considered. This allowed obtaining closed expressions that may be useful to understand the main properties of adaptive beamforming by phase coherence processing. However, real images are obtained from wideband signals, which also include some amount of noise. For the sake of simplicity, Gaussian pulses are considered, of the form:

$$s(t) = e^{-t^2/2g^2} \cos(\omega_S t + \varphi) \tag{29}$$

where the parameter g determines the bandwidth at -6 dB as a function of the relative bandwidth BW and the fundamental frequency as:

$$g = \frac{\sqrt{8\ln(2)}}{\omega_S \cdot BW} \approx \frac{2.355}{\omega_S \cdot BW} \tag{30}$$

Furthermore, signals are contaminated with noise, considered white with a Gaussian distribution. From the point of view of phase coherence processing, the duration of the ultrasonic pulse T_P relative to the signal period T_S is determined by its bandwidth and the signal-to-noise ratio. It has been shown [Camacho, 2010] that this relationship is:

$$\frac{T_P}{T_S} \approx \frac{1}{BW}\sqrt{\ln\left(\frac{SNR}{2.1}\right)} \tag{31}$$

Figure 11 shows an example for an array with N=64 elements, d=$\lambda/2$, f_S = 5 MHz, BW=0.6 and SNR = 30 dB. The signal received by an element is shown in (a), with its instantaneous phase in (b). The *FCC* obtained from the set of 64 signals is shown in (c). The red lines delimit the pulse duration as indicated by (31). It is seen that *FCC* is higher than 0.5 within this interval, reaches unity at the center of the pulse and is nearly zero in other positions.
It must be highlighted that, for phase coherence processing, noise plays an important role: it provides information when some of the aperture data contain only noise whereas other show echo signals. This happens, for example, in the grating lobes for wideband signals.

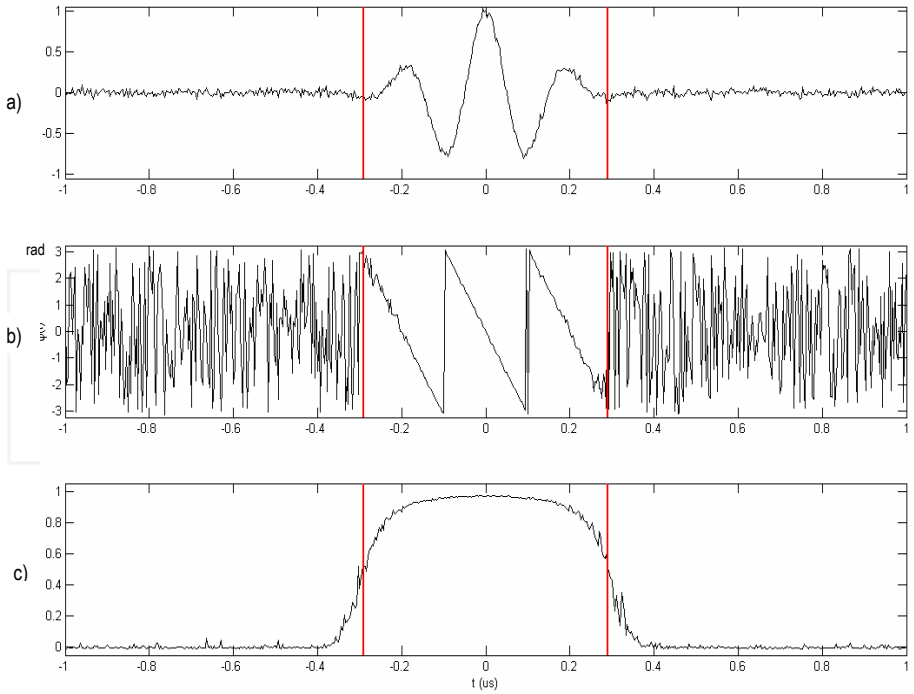

Fig. 11. a) Signal received by an element; b) Instantaneous phase; c) *FCC* of 64 signals.

Thus, since the phase dispersion of only-noise channels is high (even for low amplitude noise), the coherence factor will be small and the indication will be suppressed. This subject is further discussed in Section 8.

Figure 12 shows the 70 dB dynamic range images of a point reflector located at the far field limit ($R = D^2/4\lambda$) and θ=0º, produced by conventional beamforming (a) and after processing with *FCF* (b), *FCS* (c) and *FCC* (d). They are synthesized for an array with N=64 elements, $d=\lambda/2$, f_S = 5 MHz, BW=0.5 and with a signal-to-noise ratio SNR = 60 dB in every channel.

The sidelobe indications in the original image are suppressed by more than 50 dB with phase or sign coherence processing. Besides, the -6 dB lateral resolution has improved by nearly 50%. Processing with the complex coherence factor *FCC* (d) produces a smooth image of the point reflector. However, the images obtained after processing with the *FCF* (b) and *FCS* (c) show a periodic pattern in the main lobe as well as in the residual side lobes.

Noise is not visible in these images, since it falls below the image dynamic range after beamforming of the 64 channels.

7. Filtering out the periodic artifacts

The lateral patterns of phase $FCF(\theta)$ and sign $FCS(\theta)$ coherence factors depend on the focus position as it has been shown. To analyze more in detail this effect, Figure 13 shows the beamformed A-scan signal (blue) together with the *FCF* (green) and *FCS* (red) for the example above at θ= 0.9º, which corresponds to half the angle of the first main lobe zero (θ_{z1}).

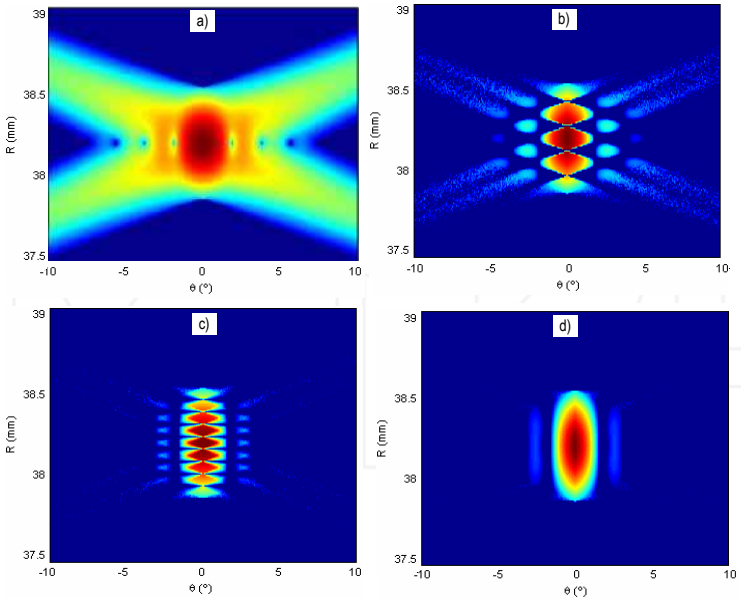

Fig. 12. Images of a point reflector obtained with conventional beamforming (a) and after processing with *FCF* (b), *FCS* (c) and *FCC* (d). Dynamic range 70 dB; N=64 elements, $d=\lambda/2$, f_S = 5 MHz, BW=0.5 and SNR = 60 dB per channel.

The amplitude of both factors changes with depth, which influences the image as shown in Fig. 12 b) and c). It can be observed that the *FCF* period of oscillation equals to that of the signal, whereas *FCS* oscillates at twice the signal frequency. This suggests that these oscillations could be reduced by a simple low-pass filter. However, low-pass filtering would provide the *average* of the coherence factors, while the *maximum* is required to keep the amplitude of the indications within the main lobe independent of depth.

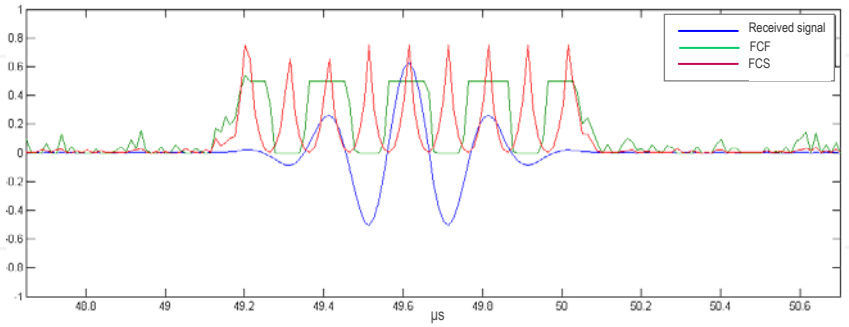

Fig. 13. Received signal (blue) and coherence factors *FCF* (green) and *FCS* (red).

A filter of ordered statistics that extracts the moving maximum [Pitas & Venetsanopoulos, 1990] seems an adequate choice. The filter output is the maximum of M consecutive samples of the coherence factor, where M is adapted to the signal frequency by means:

$$y[n] = F_v(x[n]) = \max(x[n-M+1], \ldots, x[n]), \quad M = round\left(h\frac{f_m}{f_s}\right) \tag{33}$$

being f_m the sampling frequency, h=1 for the *FCF* and h=1/2 for the *FCS*.
This non-linear filter has abrupt transitions that may be softened by means of a low-pass filter with a cutoff frequency equal to that of the signal. A moving average filter can be used with this purpose, building a combined moving maximum-average filter.
Figure 14 compares the images obtained for the same example than above without and with a moving maximum-average filter applied to the coherence factors output. The combination of both filters completely removes the periodic artifacts that appear by direct application of *FCF* and *FCS*, the lateral resolution and the sidelobe suppression remains similar to that achieved without these filters. This way, *FCF* and *FCS* behave similarly to *FCA* and *FCC*.

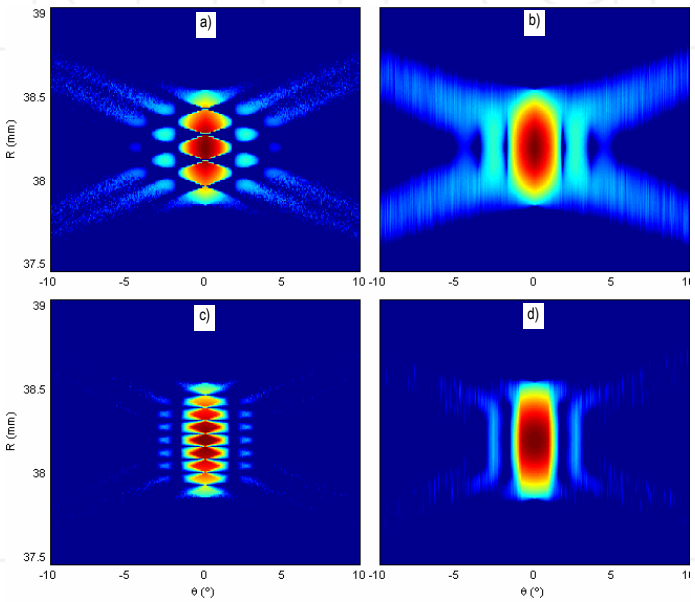

Fig. 14. 70 dB images of a point reflector: a) *FCF* processing; b) *FCF* processing with filters; c) *FCS* processing; d) *FCS* processing with filters. Filters (moving maximum + average).

8. Grating lobes suppression

When the inter-element distance is $d>\lambda/2$, grating lobe artifacts appear as a consequence of the spatially undersampled aperture (an aliasing effect). In the far field with monochromatic wave, a grating lobe is indistinguishable from the main lobe, since all the array elements contribute to its formation with the same phase at a given angular direction. With wideband signals and in the aperture near field, only a subset of the array elements produces the grating lobe at a given location. This way, with wideband signals, grating lobes spread over a large region and their amplitude is significantly lower.

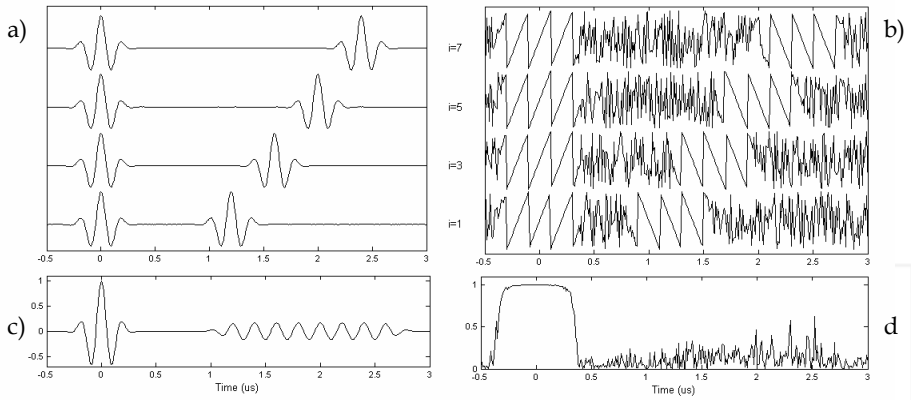

Fig. 15. Principles of grating lobes suppression: a) Aperture data amplitudes and b) phases; c) beamformer output; d) Phase coherence factor *FCF*

In fact, at a grating lobe, most of the aperture data are noise and only a few elements contribute constructively to the coherent sum. This opens an opportunity to cancel the grating lobe artifacts by phase coherence processing. To demonstrate its operation, Figure 15a) shows the aperture data corresponding to 4 channels of an 8-element array. At the left part of the A-scans, a true scatterer is located at the focus, whereas the rightmost indications correspond to a grating lobe. It is seen that all the aperture data contribute constructively to form the output A-scan in the true scatterer, but only a fraction of the aperture data adds constructively at the grating lobe (Fig. 15c).

In conventional beamforming, grating lobes show as relatively low level indications that spread out spatially (over directions and time). However, consider the aperture data phases for the same example (Fig. 15b). They are perfectly aligned at the true scatterer position, showing a large disparity at the grating lobe indications, mainly caused by noise. The coherence factor will be large (near unity) at the true scatterer and low (near zero) at the grating lobe, as it is shown for the *FCF* in the lower trace (Fig. 15d).

The grating lobe suppression level is a function of the signal bandwidth and number of aperture data used to compute the coherence factor. Figure 16 shows these results for an array with inter-element pitch of 1.5λ. It is seen that, for N=128 and *FCC* or *FCS* processing, the grating lobes become suppressed by about 40 dB if the signal BW > 60%.

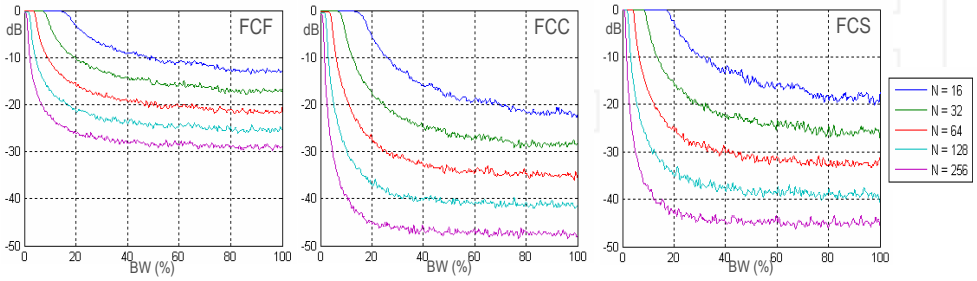

Fig. 16. Grating lobes attenuation level as a function of the signal bandwidth and number N of aperture data channels used to compute the different coherence factors.

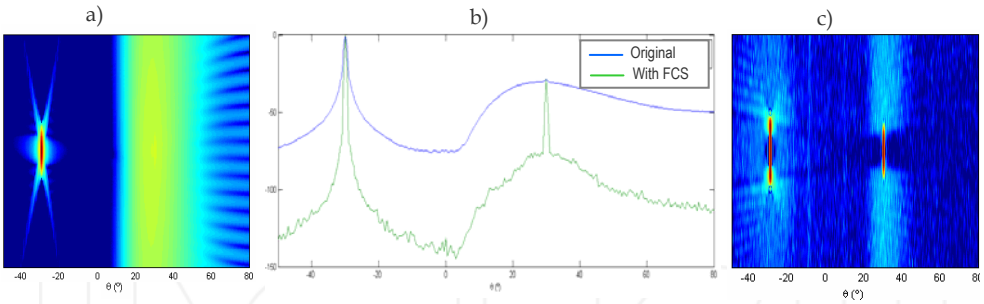

Fig. 17. a) Conventional STA image of two reflectors of 0 dB and -43 dB amplitude, obtained with a 64-element array, $d=\lambda$; b) LSF of the original and processed images; c) *FCS* image.

Figure 17a) shows the 70 dB dynamic range conventional image of two point reflectors of different amplitudes: 0 dB and -43 dB, located at angles of -30º and +30º, respectively. The images were obtained by simulation of a 5 MHz, 64-element array, $d=\lambda$, BW=50% and rms noise level of -60 dB. The modality is Synthetic Transmit Aperture (STA) [Gammelmark & Jensen, 2003], with a complete data set was used for beamforming.

It is seen that the grating lobe created by the high intensity point reflector completely hides the presence of the low-level one. This is made more evident by plotting the LSF (maximum amplitude at all depths), shown in Fig. 17b). In the original image, the grating lobe reaches a level similar to the amplitude of the smaller reflector, so that, its indication becomes literally buried in this artifact. But, after processing with the *FCS*, both point reflectors appear about 40 dB above the residual sidelobe level at, approximately, -80 dB.

Figure 17c) shows the image of the sign coherence factor, *FCS*, also with a 70 dB dynamic range. It is seen that it reaches unity (0 dB) at *both* reflector positions. Although this image gives no amplitude information, it determines the presence of true reflectors, even in the case of their signal amplitudes being below the grating lobe level.

By the way, the resulting lateral resolution produced by phase coherence processing of this 64-element sparse aperture is higher than that obtained with a 128-element dense aperture.

9. Limits on the grating and sidelobes suppression level

Out of the main lobe, the aperture data phases behave as a random variable, uniformly distributed in $(-\pi, \pi]$. The coherence factors have been defined to be zero when the phases distribute uniformly, so that they approach zero in the sidelobe region. However every coherence factor tends to this limit differently as a function of the number n of the phase values involved in its evaluation (in *phased array* $n=N$, the number of aperture data samples). This dissimilar behavior explains the differences in the sidelobe and grating lobe suppression levels achieved by every coherence factor.

For the phase coherence factor *FCF*, defined in (23) as:

$$FCF = \max\left(0\,, 1-\frac{\sigma_\varphi}{\sigma_0}\right) \quad \sigma_\phi(n) = \sqrt{\frac{\sum_{i=1}^{n}(\varphi_i-\overline{\varphi})^2}{n}} = f(n^{-1/2}) \tag{34}$$

$$\lim_{n\to\infty}\sigma_\varphi(n) = \sigma_0 \tag{35}$$

$$FCF\big|_{sidelobes} \to 0 \quad as \quad f(n^{-1/2}) \tag{36}$$

For the complex coherence factor *FCC*, defined in (20) and (21) as,

$$FCC = 1 - \sqrt{\mathrm{var}(\cos\varphi) + \mathrm{var}(\sin\varphi)} \tag{37}$$

$$\mathrm{var}(\cos\varphi) = \frac{1}{n}\sum_{i=1}^{n}\cos^2\varphi_i - \frac{1}{n^2}\left(\sum_{i=1}^{n}\cos\varphi_i\right)^2 \tag{38}$$

$$\mathrm{var}(\sin\varphi) = \frac{1}{n}\sum_{i=1}^{n}\sin^2\varphi_i - \frac{1}{n^2}\left(\sum_{i=1}^{n}\sin\varphi_i\right)^2 \tag{39}$$

$$\mathrm{var}(\cos\varphi) + \mathrm{var}(\sin\varphi) = \frac{1}{n}\sum_{i=1}^{n}(\sin^2\varphi_i + \cos^2\varphi_i) - \frac{1}{n^2}\sum_{i=1}^{n}(\sin\varphi_i + \cos\varphi_i) \tag{40}$$

With $\sin^2 x + \cos^2 x = 1$ and $|\sin x + \cos x| \le \sqrt{2}$ the second term is bounded by κ/n, κ=constant and,

$$\mathrm{var}(\cos\varphi) + \mathrm{var}(\sin\varphi) = 1 - \frac{\kappa}{n} \tag{41}$$

$$FCC = 1 - \sqrt{1 - \frac{\kappa}{n}} \approx \frac{\kappa}{2n} = f(n^{-1}) \tag{42}$$

The sign coherence factor, *FCS*, was defined in (28) as:

$$FCS = 1 - \sqrt{1 - \left(\frac{1}{n}\sum_{i=1}^{n} b_i\right)^2}$$

Among the aperture data polarity bits b_i, there will be p positive values and n-p negative values. Then,

$$B = \frac{1}{n}\sum_{i=1}^{n} b_i = \frac{p - (n-p)}{n} = \frac{2p}{n} - 1 \tag{43}$$

$$FCS = 1 - \sqrt{1 - B^2} = 1 - \frac{2p}{n}\sqrt{\frac{n}{p} - 1} \tag{44}$$

For uniform phase distributions, $p \to n/2$ and the square root term tends to unity. Therefore,

$$FCS \to 1 - \frac{2p}{n} = f(n^{-1}) \tag{45}$$

In summary, *FCC* and *FCS* approach zero following a function $f(n^{-1})$, which is stronger than the trend towards zero shown by *FCF* as $f(n^{-1/2})$.

10. Experimental verification

The validity of the adaptive beamforming technique to improve lateral resolution, dynamic range, signal-to-noise ratio and artifact suppression is experimentally demonstrated.

In a first arrangement, an aluminum block with 10 pairs of 1.5 mm Ø side drilled holes (SDH) was used (Fig. 18). This part is mainly intended to test the resolution improvement together with sidelobe and reverberation artifacts reduction.

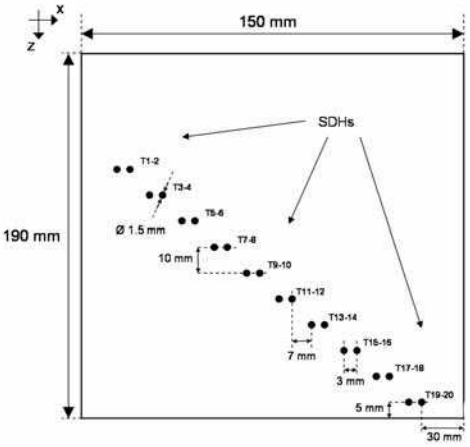

Fig. 18. Aluminum block with several pairs of side drilled holes.

A 5 MHz, 128-element array with d=0.6 mm (≈λ/2) (Imasonic, Besançon, France) was used in contact with the part upper surface. A SITAU 128:128 full parallel phased array system (Dasel, Madrid, Spain), was used to generate and acquire ultrasound data. The STA modality was applied for imaging, with dynamic focusing in emission and in reception.
Figure 19 shows the 80 dB dynamic range image obtained by conventional beamforming. Besides the indications of the SDHs, the image shows the sidelobes and reverberations produced among them and the part walls. Also, a small amount of noise is seen above the SDH indications (electrical noise). The bottom echo of the part is also clearly visible.

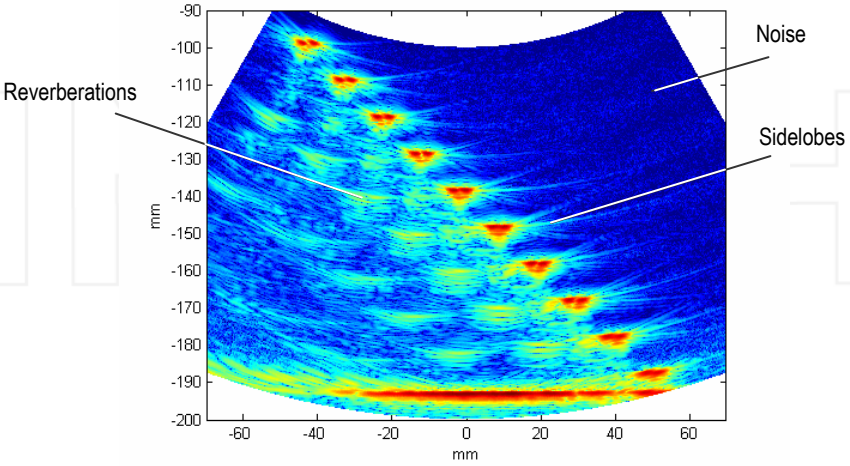

Fig. 19. STA image of the aluminum block with SDH obtained with 80 dB dynamic range

Coherence factors were computed from the aperture data following the procedures described in this paper, being applied to the whole set of N^2 signals provided by the STA imaging modality.

Figure 20 shows the 80 dB dynamic range images that result after weighting the beamformer output with a) *FCF*, b) *FCC*, c) *FCA* and d) *FCS*. The following observations can be made:

1. All the coherence factors provide a large suppression of the noise and reverberation artifacts, being moderate with *FCF* and complete with *FCA*.
2. Sidelobe indications get also fully suppressed with *FCA*, leaving some residual traces with *FCC* and *FCS* and slightly higher with *FCF*.
3. In the negative side, the *FCA* completely removes the bottom echo and its nearest SDH indications. This is due to the mutual interferences between the corresponding echoes that lower the strict coherence factor *FCA*, applied to 128^2 aperture data phases. This effect also causes some amplitude loss in the bottom echo with *FCC*, *FCS* and *FCF*.

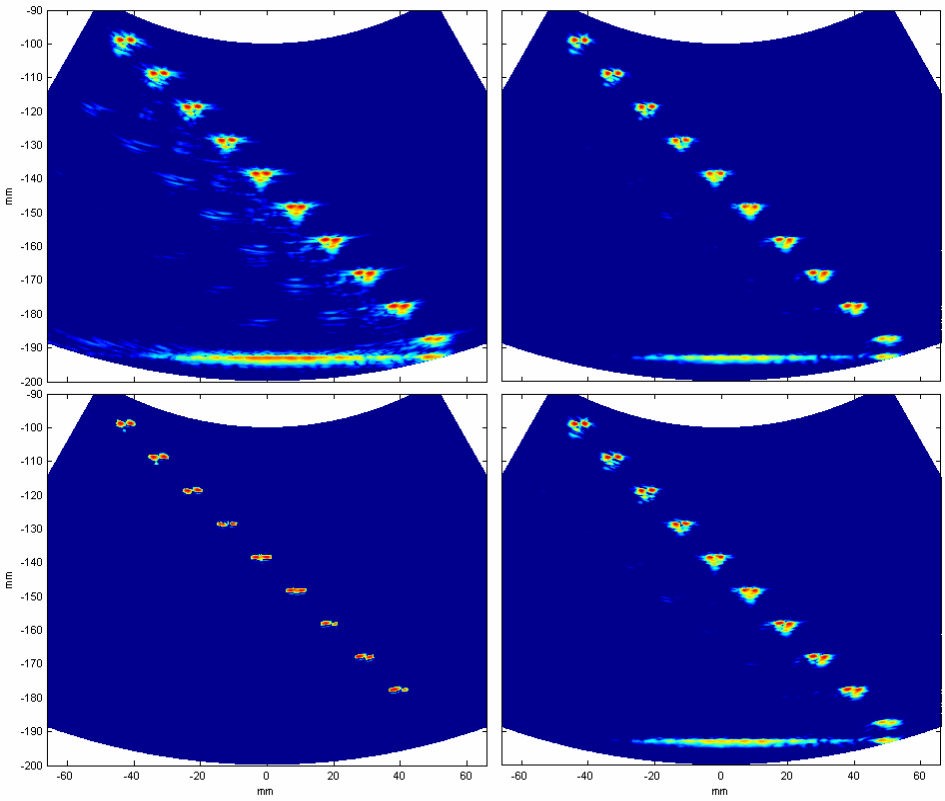

Fig. 20. Images obtained after processing with the coherence factors: a) *FCF*, b) *FCC*, c) *FCA* and d) *FCS*. Dynamic range: 80 dB.

The last observation advises of not using global processing with the STA imaging modality, due to the risk of losing some indications (especially with *FCA*). It seems better to apply the phase coherence processing to every one of the *N* partial images and keep the maximum

coherence found to perform the weighting operation, at the expenses of a lower sidelobe and artifact reduction.

With regard to the lateral resolution improvement achieved by the adaptive beamforming technique, Figure 21 shows the images (in a linear color scale) before and after the weighting operation with different coherence factors for the three central pairs of SDH, where the angular interval between two holes is about 1.1º. Since the theoretical main lobe width is, for this aperture, about 1.8º, the original image cannot fully resolve their indications.

However, after the weighting operation with the different coherence factors, the SDH indications become separated, due to the narrowing effect on the main lobe width (discussed in Section 3).

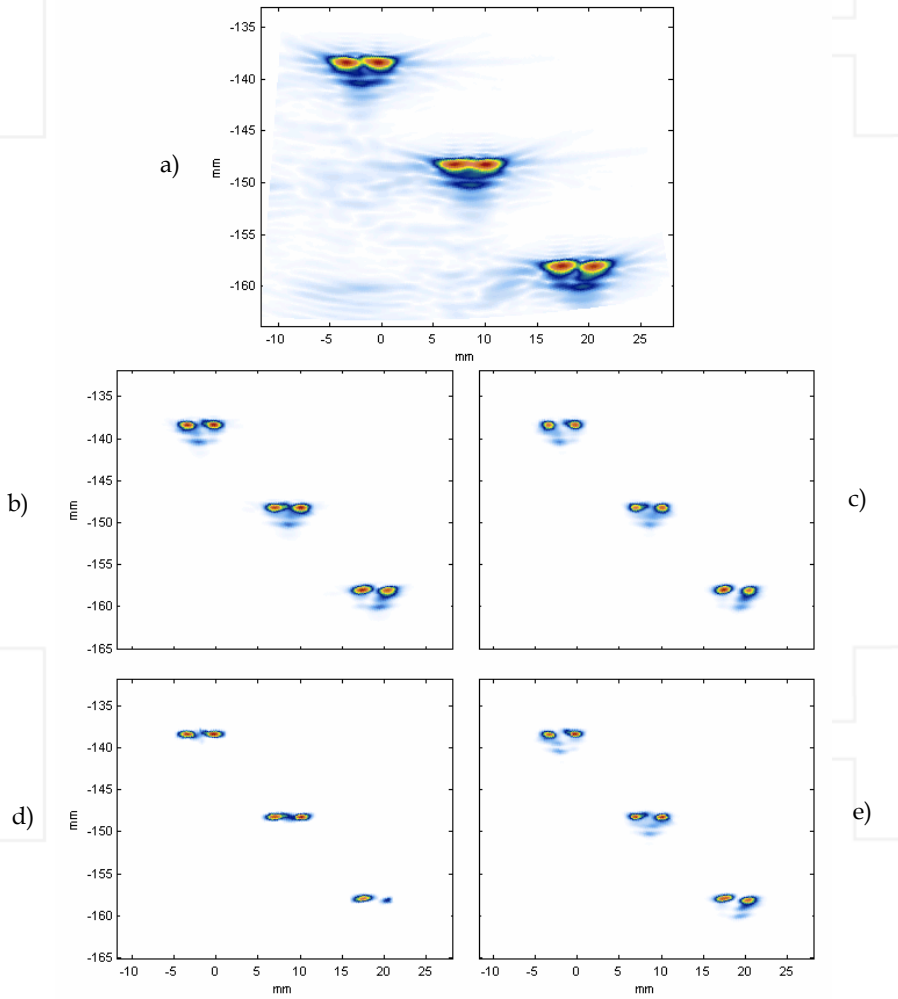

Fig. 21. Images of the three central pairs of SDH in linear scale: a) Original and processed with: b) *FCF*; c) *FCC*; d) *FCA*; e) *FCS*.

Table 1 shows the number of SDH pairs which become resolved at a given threshold.

	Number of SDH pairs resolved			
	-3 dB	*-6 dB*	*-12 dB*	*-20 dB*
Original	9	7	1	0
FCF	10	10	8	2
FCC	10	10	9	5
FCA	9	9	8	7
FCS	10	10	9	4

Table 1. Number of SDH resolved at a given threshold.

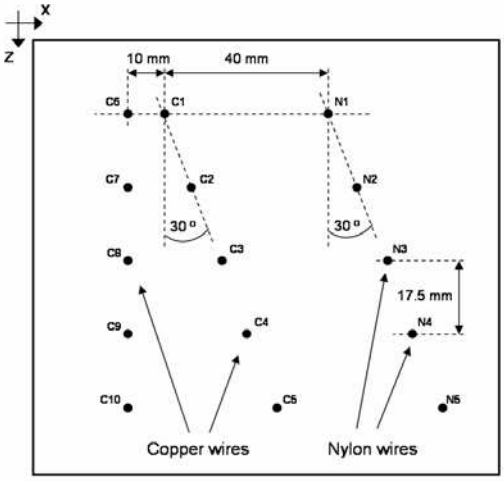

Fig. 22. Wire phantom.

Processing with any coherence factor (except *FCA*), resolves all the SDH pairs at -6 dB, whereas in the original image 3 pairs remain unresolved. At -20 dB, processing with the *FCA* resolves 7 pairs of SDH, while all pairs get unresolved in the original image.

The aim of a second experiment is to demonstrate the capabilities of the new technique to suppress grating lobes. To this purpose, a phantom with several nylon and copper wires was built (Fig. 22). The test is performed in water immersion with a 5 MHz, 96-element array with an inter-element pitch d = 0.5 mm ≈ 1.7λ. The SITAU 128:128 full parallel phased array system was used to generate and acquire the ultrasound data.

Figure 23a shows the image generated with the STA technique with a 90 dB dynamic range. The grating lobe artifacts created by the copper wires show at the right as large diffuse regions that hide the presence of some nylon wires. Conversely, the grating lobes created by the nylon wires appear at the left of the image. In this case their level is not enough to hide the presence of the copper wires. Sidelobe indications are also present, as well as some electrical noise.

The coherence factors were computed from the aperture data, using the whole set of N^2 signals and following the procedures presented in this paper. As an example, figure 23b) shows the 90 dB image of the *FCS*, before performing the weighting operation. It can be appreciated the high intensity (nearly 0 dB) at the wire positions and the high level of suppression of the grating lobes, even in a larger degree than the side lobes.

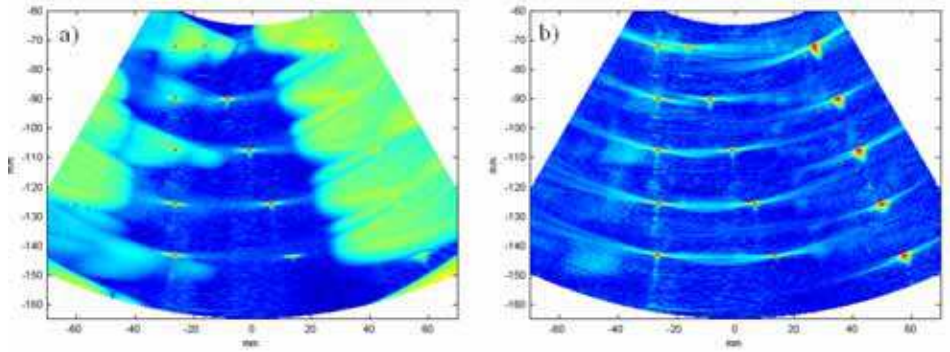

Fig. 23. a) STA image of the wire phantom; b) FCS image. Dynamic range = 90 dB

Figure 24 summarizes the images obtained after application of the different coherence factors. As expected, the grating and side lobe suppression level is higher with *FCA*, which also loses several target indications. As before, *FCA* processing is not advisable with STA.
In the reverse side, the *FCF* provides lower grating and sidelobe suppression levels, in agreement with the behavior discussed in Section 9. Both, *FCC* and *FCS*, suppress grating

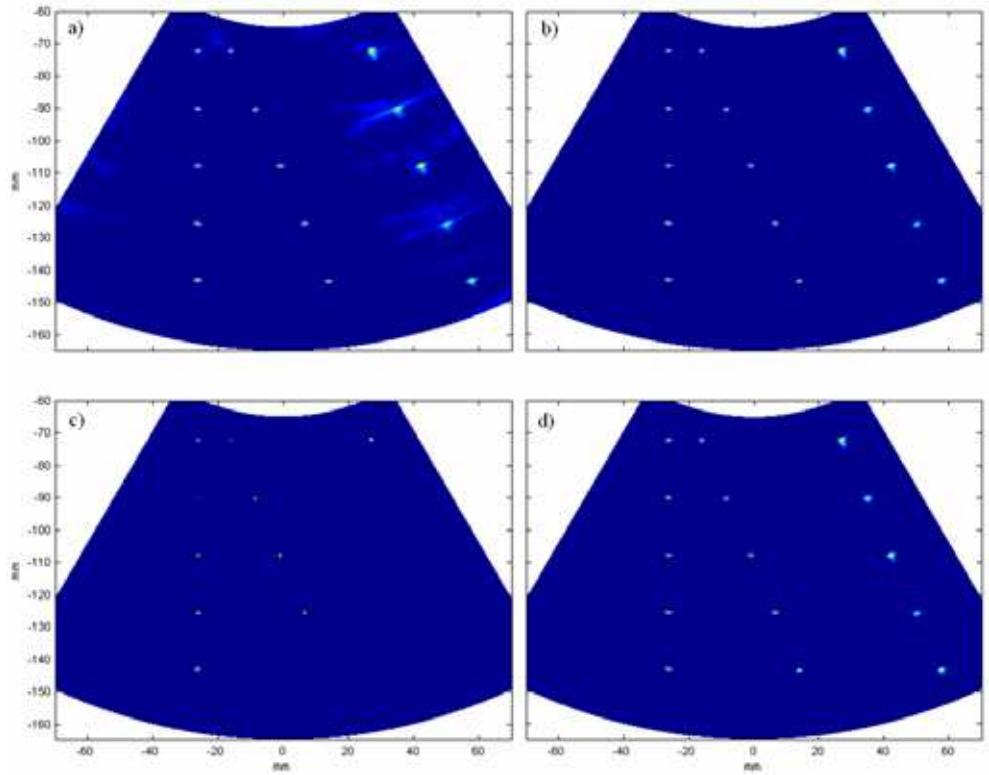

Fig. 24. Images after processing with the coherence factors: a) *FCF*, b) *FCC*, c) *FCA*; d) *FCS*.

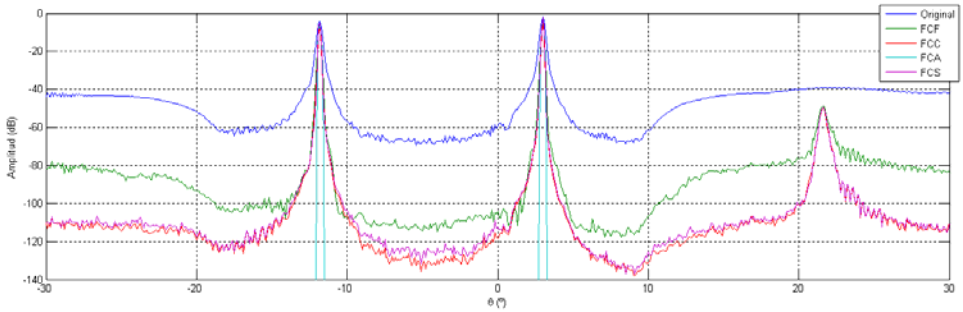

Fig. 25. LSF of the images before and after processing with different coherence factors.

and side lobe indications to well below -90 dB. It is worth to note these similarities in spite of the very different real-time implementation complexity involved.

Dramatic contrast improvements are obtained, as shown explicitly by the LSF applied to the fourth wire row (Fig. 25). The similarities in the results provided by *FCC* and *FCS* processing are made more evident, achieving a signal-to-grating lobe ratio enhancement approaching 60 dB. On average the signal-to-grating lobe ratio is raised to 63, 84 and 83 dB with *FCF*, *FCC* and *FCS* processing, respectively, from an original value of 28.5 dB.

11. Conclusion

This work describes a new ultrasonic imaging modality by means of adaptive beamforming with phase coherence processing. From the aperture data phases dispersion, it extracts a coherence factor with values in the [0, 1] interval that provides a quantitative measurement of the focusing quality: It yields a high value (≈ 1) if the received signals come from the focus and a low value (≈ 0) if they proceed from other regions. The coherence factors modify the behavior of the beamformer by weighting its output. This way, the indications produced by side and grating lobes, as well as other artifacts such as reverberations and noise, become suppressed. Besides, lateral resolution improvements are also obtained.

Four coherence factors have been defined, namely: the absolute phase coherence factor *FCA*, which operates on unwrapped phases, the complex phase coherence factor *FCC*, which considers the phases having a circular distribution, the phase coherence factor *FCF*, which regard the phases having a linear distribution in $(-\pi, \pi]$, and the sign coherence factor *FCS*, which quantify the aperture data phases with a single bit. Their main properties, including the grating and side lobe suppression degree provided by the different coherence factors have been analyzed for monochromatic, noise-free waves, as well as for wideband, noisy signals. Experimental results agree with theory.

12. Acknowledgements

Work supported by projects Artemis (2010-0607) funded by the Community of Madrid and DPI2010-17648 funded by the Spanish Ministry for Science and Innovation.

13. References

Camacho, 2009: J. Camacho, M. Parrilla, C. Fritsch, Phase Coherence Imaging, *IEEE Trans. UFFC*, 56, 5, pp. 958-974, 2009.

Camacho, 2010: J. Camacho, Imagen ultrasónica por coherencia de fase, Ph. D. Thesis, *Univ. Complutense*, Madrid, 2010.

Fisher, 1993: N.I. Fisher, Statistical analysis of circular data, Cambridge Univ. Press, 1993.

Gammelmark, 2003: K. L. Gammelmark, J. A. Jensen, Multielement Synthetic Transmit Aperture Imaging using Temporal Encoding, *IEEE Trans. Medical Imaging*, 22, 4, pp. 552-563, 2003.

Gavrilov, 1997: L. R. Gavrilov, J. W. Hand, P. Abel and C. A. Cain: A Method of Reducing Grating Lobes Associated with an Ultrasound Linear Phased Array Intended for Transrectal Thermotherapy, *IEEE Trans. Ultrason., Ferroelect., Freq. Contr.*, 44, 5, pp. 1010-1017, 1997.

Gustafsson, 1993: M. G. Gustafsson, T. Stepinski, Split-Spectrum Algorithms Rely on Instantaneous Phase Information- A Geometrical Approach, *IEEE Trans. UFFC*, 40, 6, pp. 659-665, 1993.

Lockwood, 1996: G. R. Lockwood, P. C. Li, M. O'Donnell, F. S. Foster, Optimizing the Radiation Pattern of Sparse Periodic Linear Arrays, *IEEE Trans. UFFC*, 43, 1, pp. 7-14, 1996.

Lockwood, 1998: G. R. Lockwood, J. R. Talman, S. S. Brunke, Real-time Ultrasound 3D-Imaging Using Sparse Synthetic Aperture Beamforming, *IEEE Trans. UFFC*, 45, 4, pp. 980-988, 1998.

Newhouse, 1982: V. L. Newhouse, N. M. Bilgutay, J. Saniie, E. S. Furgason, Flaw-to-grain echo enhancement by split-spectrum processing, *Ultrasonics*, 20, pp. 59-68, 1982.

Nikolov, 2000: S. I. Nikolov, J. A. Jensen, Application of different spatial sampling patterns for sparse array transducer design, *Ultrasonics*, 37, pp. 667-671, 2000.

Nikolov, 2005: M. Nikolov, V. Behar, Analysis and optimization of synthetic aperture ultrasound imaging using the effective aperture approach, *Int. J. Information Theory & Applications*, 12, pp. 257-265, 2005.

Oppenheim, 1989: A. Oppenheim, R. Schaffer, Discrete-time signal processing, *Prentice Hall*, 1989.

Pitas, 1995: I.Pitas, A. N. Venetsanopoulos: Non linear digital filters, *Kluwer Academic Publishers*, Massachusetts, 1995.

Ranganathan, 2004: K. Ranganathan, M. K. Santy, T. N. Blalock, J. A. Hossack, W. F. Walker, Direct Sampled I/Q Beamforming for Compact and Very Low-Cost Ultrasound Imaging, *IEEE Trans. UFFC*, 51, 9, pp. 1082-1094, 2004.

Shankar, 1985: P. M. Shankar, V. L. Newhouse, Speckle Reduction with Improved Resolution in Ultrasound Imaging, *IEEE Trans. Son. Ultrason.*, 32, 4, pp. 537-543, 1985.

Steinberg, 1976: B. D. Steinberg, Principles of Aperture and Array System Design, *John Wiley & Sons*, 1976.

Szabo, 2004: T. L. Szabo, Diagnostic ultrasound imaging, *Elsevier Academic Press*, 2004.

Turnbull, 1991: D. H. Turnbull and F. S. Foster, Beam steering with pulsed two-dimensional transducer array, *IEEE Trans. UFFC.*, vol. 38, no. 4, pp. 320–333, 1991.

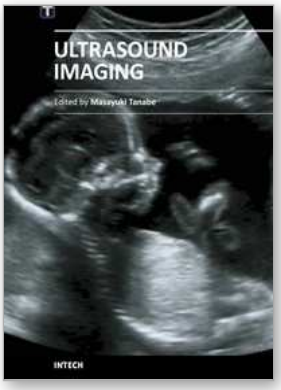

Ultrasound Imaging

Edited by Mr Masayuki Tanabe

ISBN 978-953-307-239-5
Hard cover, 210 pages
Publisher InTech
Published online 11, April, 2011
Published in print edition April, 2011

In this book, we present a dozen state of the art developments for ultrasound imaging, for example, hardware implementation, transducer, beamforming, signal processing, measurement of elasticity and diagnosis. The editors would like to thank all the chapter authors, who focused on the publication of this book.

How to reference

In order to correctly reference this scholarly work, feel free to copy and paste the following:

J. Camacho and C. Fritsch (2011). Adaptive Beamforming by Phase Coherence Processing, Ultrasound Imaging, Mr Masayuki Tanabe (Ed.), ISBN: 978-953-307-239-5, InTech, Available from: http://www.intechopen.com/books/ultrasound-imaging/adaptive-beamforming-by-phase-coherence-processing

INTECH
open science | open minds

InTech Europe
University Campus STeP Ri
Slavka Krautzeka 83/A
51000 Rijeka, Croatia
Phone: +385 (51) 770 447
Fax: +385 (51) 686 166
www.intechopen.com

InTech China
Unit 405, Office Block, Hotel Equatorial Shanghai
No.65, Yan An Road (West), Shanghai, 200040, China
中国上海市延安西路65号上海国际贵都大饭店办公楼405单元
Phone: +86-21-62489820
Fax: +86-21-62489821